



1
2
3
4
5
6
7
8
9
10
11
12
13
14
15
16
17
18
19
20
21
22
23
24
25
26
27
28
29
30
31
32
33
34
35
36
37
38
39
40
41
42
43
44
45
46
47
48

Characterization and application of artificial light sources for nighttime aerosol optical depth retrievals using the VIIRS Day/Night Band

Jianglong Zhang¹, Shawn L. Jaker¹, Jeffrey S. Reid², Steven D. Miller³, Jeremy Solbrig³, and Travis D. Toth⁴

¹Department of Atmospheric Sciences, University of North Dakota, Grand Forks, ND, USA

²Marine Meteorology Division, Naval Research Laboratory, Monterey, CA, USA

³Cooperative Institute for Research in the Atmosphere, Colorado State University, Fort Collins, CO, USA

⁴NASA Langley Research Center, Hampton, VA, USA

Corresponding Author: jzhang@atmos.und.edu



Abstract

49

50

51 Using nighttime observations from Visible/Infrared Imager/Radiometer Suite (VIIRS) Day/Night
52 band (DNB), the characteristics of artificial light sources are evaluated as functions of observation
53 conditions and incremental improvements are documented on nighttime aerosol retrievals using
54 VIIRS DNB data on a regional scale. We find that the standard deviation of instantaneous radiance
55 for a given artificial light source is strongly dependent upon the satellite viewing angle, but is
56 weakly dependent on lunar fraction and lunar angle. Retrieval of nighttime aerosol optical
57 thickness (AOT) based on the novel use of these artificial light sources is demonstrated for three
58 selected regions (United States, Middle East, and India) during 2015. Reasonable agreements are
59 found between nighttime AOTs from VIIRS DNB and temporally adjacent daytime AOTs from
60 Aerosol RObotic NETwork (AERONET) as well as from coincident nighttime AOT retrievals
61 from the Cloud-Aerosol Lidar with Orthogonal Polarization (CALIOP), indicating the potential of
62 this method to begin filling critical gaps in diurnal AOT information at both regional and global
63 scales. Issues related to cloud, snow, and ice contamination during the winter season, as well as
64 data loss due to the misclassification of thick aerosol plumes as clouds, must be addressed to make
65 the algorithm operationally robust.



66 **1 Introduction**

67 The Visible/Infrared Imager/Radiometer Suite (VIIRS), on board the Suomi National Polar-
68 orbiting Partnership (NPP) satellite, features 22 narrow-band channels in the visible and infrared
69 spectrum. Included on VIIRS is the Day/Night band (DNB), designed to detect both reflected
70 solar energy at daytime and low light visible/near-infrared signals at nighttime (e.g., Lee et al.,
71 2006; Miller et al., 2013; Elvidge et al., 2017). Compared to the Operational Line Scan (OLS)
72 sensor on the legacy Defense Meteorological Satellite Program (DMSP) constellation, the VIIRS
73 DNB has improved response to nighttime visible signals, owing to its higher spatial resolution,
74 radiometric resolution, and sensitivity (e.g., Miller et al., 2013; Elvidge et al., 2017). The DNB,
75 unlike the OLS, is calibrated which enables quantitative characterization of nighttime
76 environmental parameters via a variety of natural and artificial light signals, including reflected
77 moon light in cloudy and cloud free regions, natural and anthropogenic emissions from forest fires,
78 volcanic eruptions, gas flares from oil fields, and artificial light sources from cities (e.g., Miller et
79 al., 2013; Elvidge et al., 2017).

80 Using nighttime observations from VIIRS/OLS over artificial light sources such as cities,
81 several studies have attempted to derive nighttime aerosol optical properties. For example, Zhang
82 et al. (2008) propose the concept of estimating nighttime aerosol optical thickness (AOT) by
83 examining changes in DMSP/OLS radiances over artificial light sources between aerosol free and
84 high aerosol loading (and cloud-free) nights. However, the OLS visible channel does not have on-
85 board calibration, which limits the use of OLS data for quantitative studying of nighttime aerosol
86 properties. VIIRS's improved spatial and spectral resolutions and on-board calibration make
87 accurate quantification of nighttime aerosol properties feasible.



88 Using VIIRS radiances over selected artificial light sources, Johnson et al. (2013) develops a
89 retrieval of nighttime AOT for selected cities. However, radiances from artificial light-free regions
90 are needed for this retrieval process. McHardy et al. (2015) proposes an improved method, based
91 on the method proposed by Johnson et al. (2013) which uses changes in spatial variations within
92 a given artificial light source for retrieving nighttime AOT. The advantage of McHardy et al.
93 (2015) is that only observations over the artificial light sources themselves are needed, eliminating
94 the need for artificial light-free regions and implicit spatial invariance assumptions of Johnson et
95 al. (2013).

96 As proof-of-concept studies, only a few selected artificial light sources have been considered
97 in those pioneering nighttime aerosol retrieval studies that utilize VIIRS observations. As
98 suggested from McHardy et al. (2015), careful studies of the characteristics of artificial light
99 sources are needed to apply the method over a broader domain. Thus, in this study, using VIIRS
100 data from 2015 over the US, Middle East, and India, we focus on answering the following
101 questions:

- 102 (1) How do radiance fields from artificial light sources vary as functions of observing
103 conditions?
- 104 (2) Are nighttime AOT retrievals using VIIRS DNB feasible on a regional basis? In
105 particular, for our selected regions, can reasonable agreement be achieved between
106 nighttime VIIRS DNB derived AOT, aerosol retrievals from Cloud-Aerosol Lidar with
107 Orthogonal Polarization (CALIOP), and approximated nighttime AOT values from
108 daytime AErosol RObotic NETwork (AERONET)?
- 109 (3) What are the limitations in the current approach that can be improved in future attempts?



110 In the current study, we do not aim to finalize the nighttime retrieval methods, but rather
111 explore existing issues, report incremental advancements, and propose revised methods for future
112 studies. This paper is organized as follows: Section 2 introduces the datasets used in this study as
113 well as data processing and aerosol retrieval methods. Section 3 discusses artificial light source
114 patterns as functions of viewing and lunar geometries and lunar fraction, as well as other
115 observation-related parameters. Results of regional-based retrievals are also included in Section
116 3. Section 4 closes the paper with discussion and conclusions.

117

118 **2 Datasets and Methods**

119 **2.1 Datasets**

120 Flying in a sun-synchronous polar orbit, VIIRS has a local nighttime overpass time of ~1:30
121 am. The spatial resolution of a VIIRS DNB pixel is ~750 m across the full swath width of ~3000
122 km. VIIRS DNB observes at a wavelength range of 0.5 - 0.9 μm , with a peak wavelength of ~0.7
123 μm (e.g., Miller et al., 2013). VIIRS differs from its ancestor, OLS, by providing on-board
124 calibration for tracking signal degradation as well as changes in modulated spectral response
125 function through the use of a solar diffuser (e.g., Chen et al., 2017). Early versions of VIIRS DNB
126 data suffer from stray light contamination (e.g., Johnson et al., 2013). These issues have since
127 been corrected for in the later version of the VIIRS DNB data (Mills et al., 2013).

128 In this study, three processed and terrain-corrected VIIRS datasets were used. The
129 VIIRS/DNB Sensor Data Record (SVDNB) includes calibrated VIIRS DNB radiance data for the
130 study as well as Quality Assurance (QA) flags for each pixel. The VIIRS Cloud Cover/Layers
131 Environmental Data Record (VCCLO) dataset was used for cloud clearing, and the VIIRS/DNB
132 Sensor Data Record Ellipsoid Geolocation (GDNBO) dataset was used for obtaining geolocation



133 for the VIIRS DNB radiance data. The GDNBO dataset also includes other ancillary parameters
134 including solar, lunar, and satellite zenith/azimuth angles, as well as lunar phase that were used as
135 diagnostic information in support of this study.

136 To evaluate the VIIRS retrieved AOTs, cloud-cleared and quality-assured Level 2, Version 3
137 Aerosol RObotic NETwork (AERONET) data were enlisted as the “ground truth.” Reported in
138 AERONET data are AOTs at a typical wavelength range of 0.34 to 1.64 μm (Holben et al., 1998).
139 We point out that AERONET AOTs are derived through measuring the attenuation of solar energy
140 at defined wavelengths, and thus are only available during daytime. Therefore, averaged AOTs
141 (0.675 μm) for the day before and after the VIIRS observations were used in evaluating the
142 performance of VIIRS retrievals at night. A pair of VIIRS and AERONET retrievals are
143 considered collocated if the temporal difference is within ± 24 hours and the spatial difference is
144 within 0.4° Latitude/Longitude. All collocated AERONET data for one VIIRS data point were
145 averaged to represent the AERONET-retrieved AOT value of the desired VIIRS retrieval.

146 Nighttime aerosol retrievals are also available from CALIOP aerosol products at both regional
147 and global scales and for both day and nighttime (Winker et al., 2007). Thus, we also inter-
148 compared VIIRS nighttime AOTs retrieved from this study with CALIOP column integrated
149 AOTs. The Version 4.10, Level 2 CALIOP aerosol profile products (L2_05kmAPro) were used
150 in this study. Upon quality assurance steps, as mentioned in Toth et al. (2018), column integrated
151 CALIOP AOTs were derived at the 0.532 and 1.064 μm channels and then interpolated to the 0.70
152 μm channel (central wavelength of the DNB) for this study. The VIIRS and CALIOP data pair is
153 considered to be collocated if the spatial difference was within 0.4° Latitude/Longitude and the
154 temporal difference was within ± 1 hour. Note that one VIIRS retrieval may be associated with



155 multiple CALIOP AOT retrievals, and thus collocated CALIOP aerosol retrievals were averaged
156 to a single value for this comparison.

157 An open-source global city database from MaxMind (<http://www.maxmind.com/>) was used in
158 this study for cross checking with the detected artificial light sources for this study. The city
159 database includes the name and geolocation of the cities as well as other ancillary information.
160 Based on these data, a total of 999 cities from the Middle East region (11-42°N, 28-60°E) and
161 2995 cities from the India region (8-35°N, 68-97°E) were used in this study. These cities, as well
162 as their geolocations, are shown in Figs. 1b and 1c for the Middle East and India regions,
163 respectively, and are documented and attached as appendices to this paper.

164 One focus of this study is to understand the variations of artificial light sources as a function
165 of observing conditions. To achieve this goal, we have arbitrarily selected 200 cities across the
166 US. Since aerosol loadings are relatively low in the US compared to regions such as the Middle
167 East and India, this selection gives insight into the characteristics of artificial light sources. Also,
168 we require the selected cities to be isolated – that is, not in the immediate vicinity of another city
169 or major light source, so as to avoid light dome contamination. The majority of selected cities
170 have populations within the range of 25,000 and 100,000 with a few higher-population exceptions
171 such as Memphis, New Orleans, and Charleston. The geolocations of the 200 cities are shown in
172 Fig. 1a, and as mentioned above, the full list of the cities are also included as an attachment.

173

174 **2.2 Retrieval methods**

175 The theoretical basis for retrieving nighttime aerosol optical depth using stable artificial lights
176 is based upon previous studies (Zhang et al., 2008; Johnson et al., 2013; McHardy et al., 2015). In



177 the current approach, the VIIRS-observed radiance over a cloud free artificial light source can be
 178 expressed as:

$$179 \quad I_{sat} = I_s e^{-\tau/\mu} + I_s T(\mu) + I_p \quad (1)$$

180 Where I_{sat} is the satellite received radiance, represented as the sum of contributions from three
 181 principal components: upwelling surface light emission through direct ($I_s e^{-\tau/\mu}$) and diffuse ($I_s T(\mu)$)
 182 transmittance, and the path radiance source term (I_p). Here, τ is the total column optical depth
 183 from aerosol and Rayleigh components, μ is the cosine of the viewing zenith angle, and $T(\mu)$ is
 184 the diffuse-sky transmittance. I_s is the cloud free sky surface upward radiance, which can be
 185 further rewritten as:

$$186 \quad \pi I_s = r_s (\mu_0 F_0 e^{-\tau/\mu_0} + \mu_0 F_0 T(\mu_0) + \pi I_s \bar{r}) + \pi I_a \quad (2)$$

187 Where r_s , μ_0 , F_0 are (respectively) the surface reflectance, cosine of the lunar zenith angle, and
 188 the top-of-atmosphere downward lunar irradiance convolved with the VIIRS DNB response
 189 function. $T(\mu_0)$ is the diffuse transmittance term, \bar{r} is the reflectance from the aerosol layer, and
 190 I_a is the emission from the artificial light source. The three terms inside the parentheses of Eq. 2
 191 comprise the surface downward irradiance terms, where $\mu_0 F_0 e^{-\tau/\mu_0}$ is the downward irradiance from
 192 moonlight through direct attenuation (or $F_{directdown}$) and $\mu_0 F_0 T(\mu_0)$ is the downward irradiance from
 193 moonlight through diffuse transmittance (or $F_{diffusedown}$). The $\pi I_s \bar{r}$ term represents the surface
 194 emission (irradiance) that is reflected back downward to the surface by the aerosol layer that has
 195 a layer mean reflectivity of \bar{r} . Eq. 2 shows that the surface emission term includes emission from
 196 the artificial light source, as well as from reflected downward fluxes. Solving I_s from Eq. 2,
 197 inserting that result into Eq. 1, and rearranging, yields:

$$198 \quad I_{sat} = \frac{r_s (F_{directdown} + F_{diffusedown}) + \pi I_a}{\pi(1 - r_s \bar{r})} [e^{-\tau/\mu} + T(\mu)] + I_p \quad (3)$$

199



200

201 We expect the artificial light source emission term, I_a , to vary spatially within a heterogeneous
202 light source such as a larger city. Within that city, we can assume that the $F_{\text{directdown}}$, $F_{\text{diffusedown}}$,
203 and I_p terms have negligible spatial variations. This assumption follows McHardy et al. (2015),
204 who also assume the surface diffuse emission term ($I_s T(\mu)$) is spatially invariant. However, as
205 indicated in Eq. 3, the surface diffuse emission term includes the I_s , which contains the I_a term.
206 Thus, we retain the surface diffuse emission term in this study.

207 By taking the spatial derivative of Eq. 3 (using the delta operator Δ) and by eliminating terms
208 that have small variation within a city, we can derive:

$$209 \quad \Delta I_{\text{sat}} = \frac{\Delta I_a}{1 - \bar{r}r_s} [e^{-\tau/\mu} + T(\mu)] \quad (4)$$

210 The ΔI_a and ΔI_{sat} are the spatial variance in TOA radiance within an artificial light source for
211 aerosol and cloud free, and cloud free conditions, respectively. Similar to McHardy et al. (2015),
212 the spatial variance in radiance in this study is represented by the standard deviation of radiance
213 within an artificial light source. Also, the diffuse transmittance, $T(\mu)$, is required. Following
214 Johnson et al. (2013), we estimated the ratio (k) between direct transmittance ($e^{-\tau/\mu}$) and total
215 transmittance using the 6S radiative transfer model (Vermote et al., 1997). This approach can also
216 be shown as Eq. 5:

$$217 \quad k = e^{-\tau/\mu} / [e^{-\tau/\mu} + T(\mu)] \quad (5)$$

218 The look-up-table (LUT) values of k were computed for the AOT ranges of 0-1.5 (with every 0.05 AOT
219 interval for AOT < 0.6 and for every 0.1 AOT interval for AOT of 0.6-1.1, and with two high AOT values
220 of 1.2 and 1.5), for three different aerosol types: dust, smoke, and pollutants. We also modified the 6S
221 model (Vermote et al., 1997) to account for the spectral response function of the VIIRS DNB band (e.g.,
222 Chen et al., 2017). No sea salt aerosol was included in the LUT for this study, as artificial light sources



223 considered in this study were inland with less probability of sea salt aerosol contamination. Still, sea salt
224 aerosol can be added in later studies. Thus, we can rewrite Eq. 4 as:

$$225 \quad \tau = \mu \ln \frac{\Delta I_a}{k \Delta I_{sat} (1 - \bar{r} r_s)} \quad (6)$$

226
227 As suggested from Eq. 6, nighttime column optical thickness (τ) can be estimated using spatial
228 variances of an artificial light source over aerosol- and cloud-free conditions. The $\bar{r} r_s$ term arises from
229 the reflectance between the aerosol and the surface layers. This term is small for dark surfaces or
230 low aerosol loading cases, but could be significant for thick aerosol plumes over bright surfaces,
231 such as dust aerosols over the desert. We assume this term is negligible for this study. Note that
232 τ values from Eq. 6 include AOT as well as scattering (Rayleigh) and absorption (e.g., oxygen A
233 band) optical depth from gas species. To derive nighttime AOTs, 6S radiative transfer calculations
234 (Vermote et al., 1997) were used, assuming a standard atmosphere, to compute and remove the
235 component due to molecular scattering.

236

237 **2.3 Data pre-processing steps**

238

239 The VIIRS data pre-processing for nighttime aerosol retrievals is implemented through two
240 steps. First, artificial light sources are identified. Second, the detected artificial light sources are
241 evaluated against a known city database and a detailed regional analysis is performed. This latter
242 step is necessary to eliminate any unwanted “false” artificial light sources such as cloud
243 contamination or lightning strikes.

244 In the first step, conducted on individual ‘granules’ (~90 second orbital subsets) or composites
245 of adjacent granules, artificial light sources are selected after cloud screening and quality assurance
246 procedures. Since VIIRS nighttime aerosol retrievals assume cloud free conditions, cloud-
247 contaminated pixels must be removed using the VIIRS cloud products. Note that the nighttime
248 VIIRS cloud mask is thermal infrared based, and has its limitations in detecting low clouds



249 (especially over land), and thus additional cloud screening methods are also implemented as
250 mentioned in a later section. A single granule of VIIRS DNB radiance data is 4064 by 768 pixels
251 while, for the same VIIRS granule, the VIIRS cloud product reports values at 2032 by 384 pixels.
252 Thus, the VIIRS cloud product is first oversampled and then used to screen the radiance data.
253 Following the cloud screening step, VIIRS DNB Quality Assurance (QA) flags are used to
254 eliminate pixels that either have missing or out-of-range data, exhibit saturation, or have bad
255 calibration quality. We require the solar zenith angle to be larger than 102° to eliminate solar
256 (including twilight) contamination. Upon cloud screening and QA checks, artificial light pixels
257 are detected using a threshold based method by examining the difference in radiance of a given
258 pixel to background pixels, as suggested in Johnson et al. (2013). Artificial light pixels are defined
259 as pixels having radiance values greater than 1.5 times that of the granule or multi-granule mean
260 cloud-free background radiances.

261 The implementation of the first pre-processing step is illustrated in Figs. 2a-2d. Figure 2a
262 shows VIIRS DNB radiance data over North America for Oct. 1, 2015. Figure 2b shows the same
263 data as Fig. 2a but with cloud screening (shown in gray) and QA steps applied. Data removed by
264 the day/night terminator (i.e., solar zenith angle $< 102^\circ$) are shown in cyan, and pixels with QA
265 values indicating signal saturation are shown in yellow. Pixels in orange color in Fig. 2c are the
266 detected potential light sources on the granule scale. As shown in Fig. 2c, some cloud pixels may
267 still be misclassified as artificial light sources. To avoid such false detection, the detected artificial
268 light sources are further evaluated against a list of known cities for a given region as mentioned in
269 Section 2. This step is shown in Fig. 2d, where green colored pixels are artificial light sources
270 confirmed by the known city light source database. Here, only 200 arbitrarily selected cities in the



271 US were used, and thus some of the artificial light sources, although positively identified, were
272 not highlighted in green as they were not in the city list.

273 The granule or multi-granule mean cloud-free background radiances are used for detecting
274 artificial light sources in the first step, which may introduce an over- or under-detection of artificial
275 light sources. To refine this detection, a regionally based artificial light source detection step is
276 implemented. In this step, a bounding box is selected for each cloud-free city. The bounding
277 boxes are manually selected for 200 cities in the US and 8 cities in the Middle-East. Based on
278 experimenting, we found that most cities have a bounding box size of less than $\pm 0.3^\circ$
279 latitude/longitude, except for large cities that have a population of ~quarter-million or more,
280 depending on countries. Thus, for the remaining 991 cities in the Middle-East and 2995 cities in
281 India, to simplify the process, a $\pm 0.3^\circ$ latitude/longitude region was picked as the bounding box.
282 The bounding boxes for large cities need to be manually selected in future studies.

283 Even if a city is partially included in a bounding box, or multiple cities reside within a bounding
284 box, retrievals can still be performed, since variances of detected artificial light sources are used
285 for aerosol retrievals regardless of origins of those artificial light sources. The latitude and longitude
286 ranges of the bounding boxes for all cities used in the study are included in the attached city list
287 files. Similar steps as mentioned in the granule or multi-granule level detection scheme are
288 implemented here, but with the use of localized mean cloud-free background radiances. The
289 results from the regional detection is shown in Fig. 3. Figure 3a is the VIIRS nighttime image for
290 Sioux City, Iowa for April 13, 2015. The detected artificial light sources are shown in Fig. 3b,
291 where pixels with green color represent artificial light sources that are identified based on the local
292 detection scheme (the second step) while the pixels with orange color represent pixels identified



293 at the granule or multi-granule level (the first step) but fail on regional detection or outside the
294 bounding box.

295 Cloud contamination remains an issue in the above steps, as shown in Fig. 2c, owing to
296 limitations in the VIIRS infrared-based nighttime cloud mask. To further eliminate cities that are
297 partially covered by clouds, for a given artificial light source, nights with mean latitudes and
298 longitudes from detected light source pixels that are larger than 0.02° of the seasonally or yearly
299 mean geolocations are excluded. This process is based on the assumption that for a partially cloud
300 covered city, only a portion of the city is detected as artificial light source, and thus the mean
301 geolocations likely deviate from the multi-night composited mean geolocations. However, this
302 step may misidentify heavy aerosol plumes as cloud contaminated scenes. These nuances of city
303 light identification remain a topic of ongoing research, and for now remain as an outstanding
304 source of uncertainty in the current retrieval algorithm.

305 On each night and for each light source, the averaged radiance, its standard deviation, the lunar
306 fraction, viewing geometries, and the number of artificial light source pixels identified, are
307 reported as diagnostic information. To further avoid contamination from potential cloud / surface
308 contaminated pixels, or from pixels with erroneously high radiance values due to lightning flashes,
309 in the process of computing standard deviation the top 0.5% and bottom 10% of pixels are
310 excluded. Finally, this dataset is further used in the retrieval process.

311

312 **3. Results**

313 **3.1. Linkages between artificial lights and observing conditions**

314 As mentioned in Section 2, 200 cities within the US were arbitrarily chosen to examine the
315 properties of artificial light sources, as we expect less significant aerosol contaminations over the



316 US in comparison to other regions considered in this study. This analysis allows us to gain insight
317 on the natural variations of artificial light sources as a function of various observing parameters—
318 variations that will determine the inherent uncertainty of aerosol retrievals.

319 Cities have varying spatial light patterns, populations, and nighttime electricity usage, as well
320 as different surface conditions. To study the overall impacts of the observing conditions on
321 artificial light source patterns, the yearly mean radiance and standard deviation of the detected
322 light sources were computed for each city, regardless of observing conditions. Then, for each city
323 and for each night, the instantaneous radiance and standard deviation values were scaled based on
324 yearly mean values to derive a yearly mean normalized radiance ($N_Radiance$) and standard
325 deviation (N_R_{std}). This process was necessary to remove city-specific characteristics, making
326 feasible the comparison of artificial light source properties from different cities. Also, to remove
327 nights with cloud contamination or bad data, the yearly mean (N) and standard deviation (N_STD)
328 of the total number of light source pixels identified for a given artificial light source was computed.
329 Only nights with a number of detected light source pixels exceeding $N - 0.1 \times N_STD$ were used in
330 the subsequent analysis.

331 Figure 4a shows the plot of Julian day versus normalized radiance using data from all 200
332 cities on all available nights, regardless of the observing conditions (with the exception of totally
333 cloudy scenes, as identified by the VIIRS cloud product, which were removed). As suggested
334 from Fig. 4a, nighttime artificial light sources vary as a function of Julian day. Higher radiance
335 values were found over the Northern Hemisphere winter season (Julian days greater than 300 or
336 less than 100, corresponding to the months of November through March of the following year),
337 compared to the Northern Hemisphere spring, summer, and fall seasons. In particular, during the
338 Northern Hemisphere winter season, high spikes of radiance values were clearly visible. The



339 increase in radiance values as well frequent high spikes in radiance values during the winter season
340 may be due in part to snow and ice reflectance (modifying the surface albedo, and hence the
341 multiple scatter between the atmosphere and surface as well as augmented lunar reflectance),
342 especially for high latitude regions. Thus, snow and ice removal steps are needed for nighttime
343 aerosol retrievals on both regional and global scales. Still, upon characterizing the snow/ice cover
344 from daytime observations, retrievals may still be possible over snow/ice contaminated regions for
345 future studies.

346 Also apparent in Fig. 4a is variation in the number of non-totally cloudy observations with
347 respect to Julian day. The minimum number of non-overcast observations that passed the QA
348 checks occurs during the months of June and July, likely due to saturation QA-flagged pixels
349 (colored in yellow in Fig. 2) reaching the furthest south during those two months. VIIRS DNB
350 QA checks also label a block of pixels adjacent to the day/night terminator as pixels with bad QA
351 (e.g., the yellow colored area in Fig. 2b). Thus, during June and July, a significant portion of
352 artificial light sources at high latitudes were removed from the analysis. These QA steps are
353 retained in the process, although relaxing these QA requirements may be an option for enhancing
354 data volume over high latitudes. An assessment of the uncertainties incurred by reducing the
355 conservative nature of the QA flag is a subject of future studies.

356 Figures 4c and 4e show that the yearly mean normalized radiance, $N_Radiance$, varies as a
357 function of lunar status, including the lunar fraction and lunar zenith angle. As the lunar fraction
358 increases, the $N_Radiance$ increases, possibly due to the increase in reflected moon light. As lunar
359 zenith angle increases (i.e., the moon is less high in the sky), a decrease in the $N_Radiance$ is
360 found, indicating a reduction in downward moon light as lunar zenith angle increases. An



361 interesting relationship between the N_{Radiance} and satellite zenith angle emerges in Fig. 4g. A
362 10-20% increase in N_{Radiance} is observed for an increase of satellite zenith angle from 0 to 60°.

363 Figures 4b,d,f,h show similar analyses as Figs. 4a,c,e,g but for $N_{\text{R}_{\text{std}}}$. A similar relationship
364 between $N_{\text{R}_{\text{std}}}$ and Julian day is also found, with larger $N_{\text{R}_{\text{std}}}$ values found in winter and smaller
365 values found in the summer. Also, larger spikes of $N_{\text{R}_{\text{std}}}$, possibly due to snow and ice
366 contamination, are found in the winter season, suggesting that careful ice and snow detection
367 methods are needed for processing VIIRS DNB data over high latitudes during the winter season.
368 Still, the increase in nighttime radiance and standard deviation of radiance may also be due to the
369 increase in artificial light usage at night during the winter months, and for this reason, seasonal or
370 monthly based ΔI_a values may be needed. In contrast to the normalized radiance, insignificant
371 changes in $N_{\text{R}_{\text{std}}}$ were observed with the varying of either lunar fraction or lunar zenith angle,
372 indicating that lunar fraction or lunar zenith angle have less impact on nighttime aerosol retrievals
373 when considering $N_{\text{R}_{\text{std}}}$.

374 $N_{\text{R}_{\text{std}}}$ was found to be strongly dependent upon the satellite zenith angle, with values larger
375 than 1 observed at near 60° viewing zenith angle, likely due to the anisotropic behavior of artificial
376 light sources, as well as longer slant paths although the true reason remains unknown. To account
377 for this viewing zenith angle dependency, a correction factor c was introduced in Johnson et al.
378 (2013) in anticipation of this result. Based on Fig. 4h, the correction factor, c , specified as a
379 function of the satellite viewing zenith angle (θ), was calculated using VIIRS DNB data from 2015
380 over the 200 selected cities:

$$381 \quad c = 1.66 - 1.75 \times \cos(\theta) + 0.91 \times \cos(\theta)^2 \quad (7)$$

382 Radiance and standard deviations values from this study were further divided by c to account for
383 the viewing angle dependency.



384 Figure 5a is a scatterplot of N_{Radiance} versus $N_{\text{R}_{\text{std}}}$. A strong linear relationship is shown
385 with a correlation of 0.92, suggesting that brighter artificial light sources are typically associated
386 with larger spatial variations in radiance. Figure 5b shows the relationship between $N_{\text{R}_{\text{std}}}$ and
387 AOT using a collocated VIIRS DNB and AERONET dataset. Only data from non-winter months
388 (April-October, 2015) were considered. Since nighttime AERONET data are not available, the
389 AERONET data used for the AOT comparisons in Fig. 5b are taken from the day immediately
390 prior and after the VIIRS nighttime observations, following the same collocation method as
391 described in Section 2. Figure 5b shows correlation between $N_{\text{R}_{\text{std}}}$ values and collocated
392 AERONET AOTs, and $N_{\text{R}_{\text{std}}}$ decreases as AOT increases. As such, Fig. 5b justifies the rationale
393 for retrieving nighttime AOT using spatial variations in artificial light sources.

394

395 **3.2 Parameter quantification for nighttime aerosol optical depth retrievals**

396 As shown in Eq. 6, to retrieve nighttime AOT using VIIRS DNB, ΔI_a , ΔI_{sat} , and k values must
397 be quantified. ΔI_{sat} is the standard deviation of an artificial light source under cloud-free
398 conditions, calculated directly from VIIRS DNB data. ΔI_a is the spatial standard deviation of the
399 same artificial light source but under aerosol and cloud-free conditions. The ΔI_a shall be derived
400 over nights with minimum aerosol contamination, or in principle, from nights with the highest
401 standard deviation of radiance (R_{std}) values. However, given that some of the highest R_{std} values
402 may correspond to unscreened clouds or lightning, for a given year and for a given city we
403 computed the mean ($R_{\text{std_ave}}(30\%)$) and standard deviation ($R_{\text{std_std}}(30\%)$) of the 30% highest R_{std}
404 values. We then used the mean plus 2 times standard deviation of 30% highest R_{std} values
405 ($R_{\text{std_ave}}(30\%) + 2 \times R_{\text{std_std}}(30\%)$) to represent the ΔI_a value. Assuming a normal data distribution,
406 two standard deviations above the mean $R_{\text{std_ave}}(30\%)$ values should represent the top 1% of the



407 highest R_{std} values of all data points—providing a way to compute the highest R_{std} value while
408 simultaneously minimizing cloud and lightning contamination. Artificial light sources are
409 excluded if the ratio of $R_{\text{std_std}}(30\%)$ to $R_{\text{std_ave}}(30\%)$ is above 15%. Those artificial light sources
410 with larger variations in peak R_{std} values are likely to be associated with cities that have less stable
411 artificial light signals. Over the US, because of the concerns for ice and snow contamination as
412 mentioned in Sect. 3.1, only data from non-winter months (April-October, 2015) were used. For
413 the India and Middle East regions, snow and ice contamination is likely insignificant and thus data
414 from all months in 2015 were used.

415 As mentioned in Sect. 2.2, k values are computed using a LUT (pre-computed using the 6S
416 radiative transfer model) for dust, smoke, and pollutant aerosols. For simplicity, we assumed the
417 US, Middle East, and India regions were dominated by pollutant, dust, and smoke aerosols,
418 respectively. In future applications, k values (related to aerosol type) shall either be evaluated on
419 a regional basis, following Remer et al. (2005), or derived directly from VIIRS as mentioned in a
420 later section.

421 Cloud contamination is a long-standing challenge to passive-based satellite aerosol research
422 (e.g., Zhang et al., 2005). In this study, the VIIRS cloud product (VCCLO) was used for cloud
423 clearing of the observed VIIRS DNB scenes. However, only VIIRS Infrared channels are applied
424 for cloud detection at night (Godin and Vicente, 2015). Thus, it is possible that low level clouds,
425 unseen by the VIIRS nighttime cloud mask, may still be present in the “cloud-cleared” scenes. To
426 further exclude potential cloud contaminated artificial light sources, we have implemented
427 additional quality control steps. First, it is noted that in the presence of low clouds certain artificial
428 light source patterns may appear differently from clear-sky conditions. Thus, only nights with
429 mean geolocations of the detected artificial light sources that are within 0.02° of multi-night clear



430 sky means are used. This approach, however, will introduce issues for regions with persistent
431 cloud or thick aerosol plume coverage, such as the Uttar Pradesh state of India, which is mentioned
432 later.

433 It was noted in Sect. 3.1 that the radiance and standard deviation of radiance are strongly
434 correlated. As such, for each city and for each year, a regression relationship between radiance
435 and standard deviation of radiance values was constructed by calculating mean and standard
436 deviation of R_{std} for a given radiance range. For a given range of radiance values, R_{std} values that
437 were two standard deviations above the mean R_{std} for that range were discarded as noisy data.
438 After removing these noisy points, the same procedures were repeated to compute the regression
439 between radiance and R_{std} values for each city. The overall mean of R_{std} ($R_{\text{std_mean}}$) for the given
440 artificial light source was also computed. Data were removed if the R_{std} value was above the
441 estimated R_{std} based on radiance values using the above discussed regression plus 0.5 times
442 $R_{\text{std_mean}}$. This step was taken to further remove cloud contaminated data, but may also remove
443 scenes with thick aerosol plumes.

444

445 **3.3 Regional retrievals**

446 One of the goals of this study is to apply the proposed algorithm on a regional scale. A full
447 retrieval and evaluation, using modified schemes as identified from this paper, will be conducted
448 in follow-up research. Here, we present preliminary results conducted on a regional scale for three
449 selected regions in 2015: the US, Middle East, and India. As mentioned previously, only non-
450 winter months were used (April-October) for the US region due to concerns of snow and ice
451 contamination, while all months were included for the other two regions.



452 Figure 6a shows the comparison between retrieved nighttime AOTs from VIIRS DNB and
453 collocated daytime AERONET AOTs ($0.675 \mu\text{m}$) for the selected 200 cities for 2015. Here VIIRS
454 DNB AOTs are retrieved without using the k (diffuse transmittance) correction term mentioned in
455 Sections 2 and 3.2. A total of 368 collocated points are found with a correlation of 0.59. Figure
456 6b shows the collocated CALIOP and VIIRS nighttime AOTs, again using the retrievals without
457 correcting for the diffuse transmittance term. A correlation of 0.47 was found between CALIOP
458 AOT (interpolated to $0.700 \mu\text{m}$) and VIIRS nighttime AOT.

459 Figures 6c and 6d show retrieval comparisons similar to Figs. 6a and 6b, but revised to include
460 the k (diffuse transmittance) correction term. An over correction was found as a higher than 1
461 slope between VIIRS and daytime AERONET AOTs, indicating that the correction for diffuse
462 transmittance may be less important for low aerosol loading cases. The daytime AERONET AOT
463 may not be a fair representation of nighttime AOTs in all cases. Large uncertainties exist in
464 CALIOP extinctions and AOTs as well, due to necessary assumptions of the lidar ratios made in
465 the retrieval process (e.g., Omar et al., 2013). Therefore, significant uncertainties exist in both the
466 AERONET and CALIOP validation sources. Still, this can be improved with the use of nighttime
467 lunar photometry data that is in development from the AERONET group (e.g., Berkoff et al., 2011;
468 Barreto et al., 2013).

469 Figures 7a and 7b show scatter plots of VIIRS DNB AOTs vs. daytime AERONET and
470 nighttime CALIOP AOTs, respectively, for the Middle East for 2015, using retrievals without k .
471 A total of 999 cities were included in the study, and 368 cities were excluded for not passing the
472 stable light source check (or $R_{\text{std_std}}(30\%) / R_{\text{std_ave}}(30\%) < 15\%$) or not having 3 or more nights
473 that passed the various checks as mentioned in previous sections (both criteria are referred as the
474 stable light source requirement). A correlation of 0.64 and 0.46 was found between VIIRS and



475 AERONET and CALIOP AOTs, respectively. However, a low bias was clearly present in both
476 comparisons. Figures 7c and 7d show the VIIRS nighttime AOTs versus AERONET (day) and
477 CALIOP (night) AOTs with k included. Similar correlations are found, yet the low bias is largely
478 corrected.

479 A similar study was conducted for India. Here we separated cities in India inside and outside
480 of the Uttar Pradesh (UP) state (retrieval for the UP state is discussed later). Of a total of 2573
481 cities outside of the UP state, 1810 cities were found to satisfy the stable light source requirement.
482 Again, Figs. 8a and 8b are for VIIRS nighttime AOTs versus AERONET adjacent daytime and
483 CALIOP nighttime AOTs without k correction and Figs. 8c and 8d are the plots with the diffuse
484 transmittance (k) correction term included, for cities that were outside the UP state. In all four
485 cases, correlations of around 0.5-0.6 were found, indicating the developed algorithm has
486 reasonable skill in tracking nighttime AOTs. A low bias occurred when k was not included. When
487 k was included, a near 1-to-1 agreement is found in both Figs. 8c and 8d. This exercise reinforces
488 the notion that there is indeed a need to account for diffuse transmittance.

489 Figures 9a and 9b compares VIIRS, AERONET, and CALIOP reported AOTs for cities within
490 the UP state of India. Of a total of 421 cities, 326 passed the stable city light requirement.
491 However, a low correlation was found between VIIRS nighttime and daytime AERONET AOTs.
492 This result is not surprising, as thick aerosol plumes cover this region most times of the year, and
493 thus the derived cloud and aerosol free sky standard deviation of the artificial light sources (the
494 ΔI_a values) are not always representative of true aerosol-free cases. Therefore, a longer study
495 period, or careful by-hand analysis, may be needed for deriving ΔI_a values for regions that are
496 known to have persistent thick aerosol plume coverage.



497 Ideally, the retrievals at each light source location should be gridded and averaged to further
498 increase the signal-to-noise ratio. We have tested this concept by averaging retrievals shown in
499 Figs. 6b, 7b, and 8b into a $1^\circ \times 1^\circ$ (Latitude/Longitude) averaged dataset. Artificial light sources
500 that have less than 20 valid nights in a year were excluded to provide statistically robust estimates
501 of ΔI_a . Comparisons of $1^\circ \times 1^\circ$ (Latitude/Longitude) averaged VIIRS DNB AOT retrievals with
502 daytime AERONET data and nighttime CALIOP AOTs are shown in Figs. 6e (6f), 7e (7f), and 8e
503 (8f) for the US, Middle East, and India regions, respectively. Increases in correlations were found
504 between VIIRS and AERONET AOTs for the India regions. Marginal changes in correlations,
505 however, occurred between VIIRS and CALIOP AOTs. Although neither daytime AERONET
506 nor nighttime CALIOP AOTs can be considered as the “ground truth” for nighttime AOTs, these
507 results suggest that the newly developed method has skills in retrieving nighttime AOTs over both
508 dark and bright surfaces.

509 Figure 10 shows nighttime AOT retrievals over India for Jan. 12 and 16 of 2015, with the
510 retrievals from the UP state of India removed. Figures 10a and 10b show true color imagery from
511 Terra MODIS for Jan. 12 and 16, 2015 (obtained from the NASA Worldview through the
512 following site: <https://worldview.earthdata.nasa.gov/>). Figure 10c and 10d show the nighttime
513 images of VIIRS DNB radiance for Jan. 12 and 16, 2015. Over-plotted on Figs. 10a and 10b are
514 retrieved VIIRS nighttime AOTs, with blue, green, orange, and red representing AOT ranges of 0-
515 0.2, 0.2-0.4, 0.4-0.6, and above 0.6, respectively, using gridded data same as used for Figs. 9e-f.
516 Shown in Fig. 10a, on Jan. 12, the west portion of India was relatively aerosol-free, but a heavy
517 aerosol plume is visible around the east coast of India. Similarly, AOTs lower than 0.2 were
518 detected over western India but AOTs larger than 0.6 were found over eastern India. On Jan.16,
519 as indicated from the MODIS daytime image, a thick plume covered the western portion of India,



520 also seen in Fig. 10d via retrieved AOTs above 0.6. Also, the northeast portion of India was
521 relatively aerosol-free as indicated from both MODIS true color imagery (Fig. 10b) and VIIRS
522 nighttime AOT retrievals (Fig. 10d).

523 Based on Figs. 10c and 10d, there were many artificial light sources not used in the retrieval.
524 Those sources were excluded by various quality-control checks of the study due to such reasons
525 as potential cloud contamination, light source instability, or insufficient valid data in a year. It is
526 very likely that some valid data will be removed in this conservative filtering process. New
527 methods must be developed to restore valid data. Some ideas to this effect are presented in the
528 section to follow.

529 The diffuse correction term, k , was shown to be an important factor in reducing bias in these
530 retrievals. We compared the k corrections estimated using the 6S model (Vermote et al., 1997) as
531 well as those empirically derived from this study. By assuming CALIOP nighttime AOTs as the
532 “true” AOTs, and using VIIRS AOTs as shown in Figs. 7b and 8b as inputs, the k correction term
533 could be inferred using Eq. 6. Figure 11a shows the derived k values vs. CALIOP nighttime AOT
534 for the Middle East region. Over-plotted are the k values estimated from the 6S model (Vermote
535 et al., 1997). The two patterns show some agreement, as both the modeled and the empirically
536 derived k values are near or above 1 for CALIOP AOTs of 0.0, and below 0.5 when CALIOP
537 AOTs of ~ 1 . This behavior indicates that the 6S-modeled k correction may provide a reasonable
538 first-order estimate for dust aerosols in this region. Figure 11b shows a similar plot as Fig. 11a
539 but for the India region. A larger data spread was found between the empirically derived and
540 modeled k values assuming smoke aerosols, although the overall patterns were similar. One of the
541 possible reasons for the disparity is that unlike the Middle East region, where dust aerosols



542 dominate, the India region is subject to many other aerosol species including dust and pollutants,
543 occurring across different regions and varying with season.

544

545 **3.5 Limitations and possible improvements**

546 Although showing some skill, the retrieval algorithm examined in this study has its limitations.
547 First, most retrievals are limited to AOTs less than 1.5. This is because scenes with heavy aerosol
548 plumes can either be misclassified as clouds by the VIIRS cloud product, or removed during the
549 additional cloud screening steps introduced in this study. For heavy aerosol plumes, much larger
550 areas could be detected as “light sources” due to enhanced diffuse radiation (e.g., Figure 11), and
551 have different mean geolocations than low aerosol loadings and cloud free nights, and thus would
552 be removed due to the geolocation checks as mentioned in Section 3.2. A data loss, especially for
553 heavy aerosol cases, is experienced in this study due to those stringent data screening steps. Also,
554 for the purpose of avoiding cloud or lightning contamination in this study, ΔI_a values were not
555 derived from nights with the highest radiance or standard deviation of radiance values. Doing so
556 creates a problem for regions having frequent heavy aerosol plume loading, such as the UP state
557 of India.

558 Both issues mentioned above may be mitigated by constructing a prescribed city pattern for
559 each light source based on a multi-night composite from cloud free and low aerosol loading
560 conditions. In that case, light source pixels from the exact same location would be used each night
561 to reduce data loss, especially for nights with heavy aerosol plumes. In constructing the predefined
562 city pattern, ΔI_a values may also be derived. The construction of a prescribed city pattern will be
563 attempted in a future study.



564 Even after vigorous attempts at cloud screening, there remains some cloud contamination.
565 Such conditions may account in Figs. 6-8 for high VIIRS AOT but low CALIOP or AERONET
566 AOT cases, although both daytime AERONET data and CALIOP data have their own issues for
567 representing nighttime aerosol optical depth, as discussed. More advanced cloud screening
568 methods are needed to improve the screening-out of residual clouds. In addition, snow and ice
569 cover pose challenges for this study, and new methods need to be developed to account for snow
570 / ice coverage and allow for attempts at nighttime AOT retrievals over those scenes.

571 Even the algorithm as presented shows skill in retrieving nighttime AOT. Given that there are
572 hundreds of thousands of cities and towns across the world that could serve as sources for this
573 algorithm, the composite of retrievals from artificial light sources may provide a tractable means
574 to attaining regional to global description of nighttime aerosol conditions, on both moonlit and
575 moon-free nights, and over both dark and bright land surfaces. Considering the current glaring
576 nocturnal gap in AOT, the current results show promise for providing closure and thereby enabling
577 cloud/aerosol process studies and improved parameterizations for weather and climate modeling.
578

579 **4 Conclusions and Implications**

580 In this study, based on Visible/Infrared Imager/Radiometer Suite (VIIRS) Day/Night band
581 (DNB) data from 2015, we examined the characteristics of artificial light sources for selected cities
582 in the US, India, and the Middle East regions. Our findings point toward the following key
583 conclusions:

- 584 1. Radiance from artificial light sources is a function of time of year, lunar illumination and
585 geometry, and viewing geometry. Larger radiance values and spikes in radiance values
586 can occur during the winter season, possibly related to snow and ice cover, indicating the



587 need for careful snow and ice detection for nighttime retrievals using VIIRS data. The
588 normalized radiance increases with lunar fraction, and decreases with increasing lunar
589 zenith angle—as these parameters are tied to the magnitude of downwelling moonlight.

590 2. The normalized standard deviation of artificial light source radiance is a function of time
591 of year and similar to normalized radiance, exhibit spikes during the winter season.
592 However, no significant relationship was found between the normalized standard deviation
593 of radiance and lunar characteristics, including lunar fraction and lunar zenith angle. This
594 finding suggests that the standard deviation of radiance, as opposed to the normalized value
595 of radiance, is a potentially more robust parameter for nighttime aerosol retrievals using
596 VIIRS DNB data.

597 3. Both the normalized radiance and the normalized standard deviation of radiance are a
598 strong function of satellite viewing angle, with larger normalized radiance and the
599 normalized standard deviation of radiance values occurring at higher satellite viewing
600 angles. As anticipated by past research, this viewing angle dependency must be accounted
601 for in VIIRS DNB nighttime aerosol retrievals based on artificial light sources.

602 4. Preliminary evaluations over the US for 200 selected cities, over the Middle East for 999
603 cities/towns, and over India for 2995 cities/towns (excluding the Uttar Pradesh State of
604 India) show reasonable agreements between VIIRS nighttime aerosol optical thickness
605 (AOT) and values estimated by adjacent-daytime AEROSOL ROBOTIC NETWORK
606 (AERONET) and nighttime Cloud-Aerosol Lidar with Orthogonal Polarization (CALIOP).
607 This finding suggests that the use of artificial light sources holds the potential of being
608 viable for regional as well as global nighttime aerosol retrievals.



609 5. Poor correlation was found between VIIRS nighttime AOTs and daytime AERONET
610 AOTs for the Uttar Pradesh state in India. This region is frequently covered by thick
611 aerosol plumes, and this may introduce a difficulty in constructing cloud and aerosol free
612 night characteristics of artificial light sources (ΔI_a) for the retrieval process. Based on this
613 finding, we conclude that detailed analysis, and perhaps by-hand selection of non-turbid
614 baseline conditions, is needed for estimating ΔI_a values in regions of climatologically high
615 and persistent turbidity.

616 6. In contrast to McHardy et al. (2015), the need for a diffuse correction in the nighttime
617 aerosol retrieval process was found to indeed be important for regions with heavy aerosol
618 loadings. This study further suggests radiative transfer model based estimations of the
619 diffuse correction term compare reasonably well with empirically derived values over the
620 Middle East where the dominant aerosol type is dust. However, in cases such as the India
621 region, where several aerosol types may be expected during a year, a larger data spread
622 was found, and specification of the diffuse correction term requires additional study.

623 Despite the advances made here, there remain many limitations to the current algorithm. For
624 example, snow, ice, and cloud contamination can significantly affect the retrieved AOTs.
625 Advanced procedures for snow, ice, and cloud removal are needed, with a full evaluation for the
626 potential impacts. Also, high aerosol loading may be screened out due to misclassification of thick
627 aerosol plumes as clouds. A pattern-based artificial light source method will be examined in a
628 future study as one approach to mitigating this issue. Despite these known issues, these low-light
629 studies forge a promising new pathway toward providing nighttime aerosol optical property
630 information on the spatial and temporal time scales of value to the significant needs of the aerosol
631 modeling community in terms of regional to global nighttime aerosol property information.



632 **Acknowledgments:**

633 The support of the Office of Naval Research under grant N00014-16-1-2040 and the NOAA JPSS
634 Program Office are gratefully acknowledged. S. L. Jaker was partially supported by the NASA
635 Grant of NNX17AG52G and NSF project IIA-1355466. The global city base used in this study is
636 a free open source dataset. "This product includes data created by MaxMind, available from
637 <http://www.maxmind.com/>".

638



639 **References**

- 640 Barreto, A., Cuevas, E., Damiri, B., Guirado, C., Berkoff, T., Berjón, A. J., Hernández, Y.,
641 Almansa, F., and Gil, M.: A new method for nocturnal aerosol measurements with a lunar
642 photometer prototype, *Atmos. Meas. Tech.*, 6, 585-598, doi:10.5194/amt-6-585-2013,
643 2013.
- 644 Berkoff, T. A., Sorokin, M., Stone, T., Eck, T. F., Raymond Hoff, R., Welton, E., Holben, B.:
645 Nocturnal Aerosol Optical Depth Measurements with a Small-Aperture Automated
646 Photometer Using the Moon as a Light Source, *J. Atmos. Ocean. Technol.*, 28, 1297–1306,
647 2011.
- 648 Chen, H., Xiong, X., Sun, C., Chen, X., Chiang, K.: Suomi-NPP VIIRS day–night band on-orbit
649 calibration and performance, *J. Appl. Remote. Sens.*, 11, Article 36019,
650 <https://doi.org/10.1117/1.JRS.11.036019>, 2017.
- 651 Elvidge, C. D., Baugh, K., Zhizhin, M., Hsu, F. C., and Ghosh, T.: VIIRS Night-Time Lights,
652 *International Journal of Remote Sensing*, 38, 5860–5879, 2017.
- 653 Godin, R., and Vicente, G.: Joint Polar Satellite System (JPSS) Operational Algorithm Description
654 (OAD) Document for VIIRS Cloud Mask (VCM) Intermediate Product (IP) Software,
655 National Aeronautics and Space Administration (NASA), Greenbelt, Maryland, Goddard
656 Space Flight Center. Access on November 2, 2018
657 ([https://jointmission.gsfc.nasa.gov/sciencedocs/2015-08/474-00062_OAD-VIIRS-Cloud-](https://jointmission.gsfc.nasa.gov/sciencedocs/2015-08/474-00062_OAD-VIIRS-Cloud-Mask-IP_I.pdf)
658 [Mask-IP_I.pdf](https://jointmission.gsfc.nasa.gov/sciencedocs/2015-08/474-00062_OAD-VIIRS-Cloud-Mask-IP_I.pdf)), 2015.



- 659 Holben, B. N., Eck, T. F., Slutsker, I., Tanré, D., Buis, J. P., Setzer, A., Vermote, E., Reagan, J.
660 A., Kaufman, Y. J., Nakajima, T., Lavenu, F., Jankowiak, I., and Smirnov, A.: AERONET
661 - A Federated Instrument Network and Data Archive for Aerosol Characterization, Rem.
662 Sens. Environ., 66, 1-16, 1998.
- 663 Johnson R. S., Zhang J., Reid, J. S., Hyer, E. J., and Miller, S. D.: Toward Nighttime Aerosol
664 Optical Depth Retrievals from the VIIRS Day/Night Band, Atmos. Meas. Tech., 6, 1245-
665 1255, doi:10.5194/amt-6-1245-2013, 2013.
- 666 Lee, T.E., Miller, S.D., Turk, F.J., Schueler, C., Julian, R., Deyo, S., Dills, P., Wang, S.: The
667 NPOESS VIIRS day/night visible sensor. Bull. Am. Meteorol. Soc, 87, 191–199, 2006.
- 668 McHardy T., Zhang, J., Reid, J. S., Miller, S. D., Hyer, E. J., and Kuehn, R.: An improved method
669 for retrieving nighttime aerosol optical thickness from the VIIRS Day/Night Band, Atmos.
670 Meas. Tech., 8, 4773-4783, doi:10.5194/amt-8-4773-2015, 2015.
- 671 Miller, S.D., Straka, W., III, Mills, S.P., Elvidge, C.D., Lee, T.F., Solbrig, J., Walther, A.,
672 Heidinger, A.K., Weiss, S.C.: Illuminating the Capabilities of the Suomi National Polar-
673 Orbiting Partnership (NPP) Visible Infrared Imaging Radiometer Suite (VIIRS) Day/Night
674 Band. Remote Sens., 5, 6717–6766, 2013.
- 675 Mills, S., Weiss, S., and Liang, C.: VIIRS Day/Night Band (DNB) Stray Light Characterization
676 and Correction, Proceedings SPIE 8866, Earth Observing Systems XVIII, 88661P,
677 <https://doi.org/10.1117/12.2023107>, 2013.
- 678 Omar, A. H. and coauthors: CALIOP and AERONET aerosol optical depth comparisons: One size
679 fits none, Journal of Geophysical Research: Atmospheres, 118, 4748–4766,
680 doi:10.1002/jgrd.50330, 2013.



- 681 Remer L. A., Kaufman, Y. J., Tanré, D., Mattoo, S., Chu, D. A., Martins, J. V., Li, R.-R., Ichoku,
682 C., Levy, R. C., Kleidman, R. G., Eck, T. F., Vermote, E., Holben, B. N.: The MODIS
683 Aerosol Algorithm, Products, and Validation, *J. Atmos. Sci.*, 62, pp. 947-973,
684 [10.1175/JAS3385.1](https://doi.org/10.1175/JAS3385.1), 2005.
- 685 Toth, T. D., Campbell, J. R., Reid, J. S., Tackett, J. L., Vaughan, M. A., Zhang, J., and Marquis,
686 J. W.: Minimum aerosol layer detection sensitivities and their subsequent impacts on
687 aerosol optical thickness retrievals in CALIPSO level 2 data products, *Atmos. Meas. Tech.*,
688 11, 499-514, <https://doi.org/10.5194/amt-11-499-2018>, 2018.
- 689 Vermote, E. F., Tanré, D., Deuzé, J. L., Herman, M., and Morcrette, J. J.: Second simulation of
690 the satellite signal in the solar spectrum, 6S: an overview, *IEEE Trans. Geosci. Remote*
691 *Sens.*, 35, 675–686, 1997.
- 692 Zhang, J., Reid, J. S., and Holben, B. N.: An analysis of potential cloud artifacts in MODIS over
693 ocean aerosol optical thickness products, *Geophysical Research Letters*, VOL. 32, L15803,
694 doi:10.1029/2005GL023254, 2005.
- 695 Zhang, J., Reid, J. S., Turk, J., and Miller, S.: Strategy for studying nocturnal aerosol optical depth
696 using artificial lights, *International Journal of Remote Sensing*, 29:16, 4599-4613, 2008.
- 697 Zhang J., Reid, J. S., Campbell, J. R., Hyer, E. J., and Westphal, D. L.: Evaluating the Impact of
698 Multi-Sensor Data Assimilation on A Global Aerosol Particle Transport Model. *J.*
699 *Geophys. Res. Atmos.*, 119, 4674–4689, doi:[10.1002/2013JD020975](https://doi.org/10.1002/2013JD020975), 2014.

700

701

702

703



704 **Figure Captions**

705 **Figure 1.** Spatial distribution of (a) 200 cities over the US, b). 999 cities over the Middle East,
706 and c). 2995 cities over India, used in this study. Red dots show cities/towns from the Uttar
707 Pradesh (UP) state of India—a region of climatologically high aerosol loading.

708

709 **Figure 2.** (a) VIIRS DNB contrast-enhanced imagery centered over North America from the
710 VIIRS DNB for October, 1 2015. (b) Same as (a), but with cloud screening and quality assurance
711 steps applied for cloudy (grey), saturated pixels (yellow), and solar zenith angles $< 102^\circ$ (cyan).
712 (c) Similar to (b), but with artificial light sources identified through a granule level detection
713 (orange). (d) Similar to (c) but showing artificial light sources cross checked with a known city
714 database and through a regional level detection (green).

715

716 **Figure 3.** (a) VIIRS nighttime imagery on April 13, 2015 over Sioux City, Iowa, US. b) Similar
717 to (a) but showing detected artificial light sources using data within $\pm 0.3^\circ$ (Latitude/Longitude) of
718 the city center (green). Orange colors show the detected artificial light sources through a granule
719 level detection. Only green pixels are utilized for aerosol retrievals.

720

721 **Figure 4.** (a), (c), (e), and (g) show the normalized radiance of artificial light sources (200 selected
722 cities over the US, for 2015) as functions of Julian day, lunar fraction, lunar zenith angle, and
723 satellite zenith angle, respectively. (b), (d), (f), and (h) show the corresponding normalized
724 standard deviation of radiance for artificial light sources.

725



726 **Figure 5.** (a) Normalized radiance versus normalized standard deviation of radiance for 200 cities
727 over the US for 2015. (b) The normalized standard deviation of radiance as a function of adjacent
728 daytime AERONET AOT ($0.675 \mu\text{m}$).

729

730 **Figure 6.** (a) Scatter plot of VIIRS nighttime AOT versus adjacent daytime AERONET AOT
731 ($0.675 \mu\text{m}$) for 200 selected cities over the US for 2015. No diffuse correction is applied. (b)
732 Similar to (a) but for using nighttime CALIOP AOT ($0.7 \mu\text{m}$). (c) and (d) Similar (a) and (b) but
733 with the diffuse correction implemented. (e) and (f): Similar to Figs. 6c and 6d but for gridded
734 VIIRS data (averaged into $1^\circ \times 1^\circ$ Latitude/Longitude grids). Artificial light sources with fewer
735 than 20 nights that passed various cloud screening and QA checks are excluded.

736

737 **Figure 7.** Similar to Fig. 6 but for 999 cities over the Middle East for 2015.

738

739 **Figure 8.** Similar to Fig. 7 but for the India region for 2015. Artificial light sources from the
740 Uttar Pradesh State of India are excluded.

741

742 **Figure 9.** (a) Scatter plot of VIIRS nighttime AOT versus adjacent day time AERONET AOT
743 ($0.675 \mu\text{m}$) over the Uttar Pradesh State of India for 2015. Diffuse correction is applied. (b):
744 similar to (a), but for using nighttime CALIOP AOT ($0.7 \mu\text{m}$).

745

746 **Figure 10.** Terra MODIS true color imagery (NASA Worldview) for Jan. 12, 2015 over India.
747 (b): Similar as (a) but for Jan. 16, 2015. (c): VIIRS nighttime imagery on Jan. 12, 2015. Over
748 plotted are VIIRS nighttime AOT retrievals in $1^\circ \times 1^\circ$ (Latitude/Longitude) grid format. Blue,

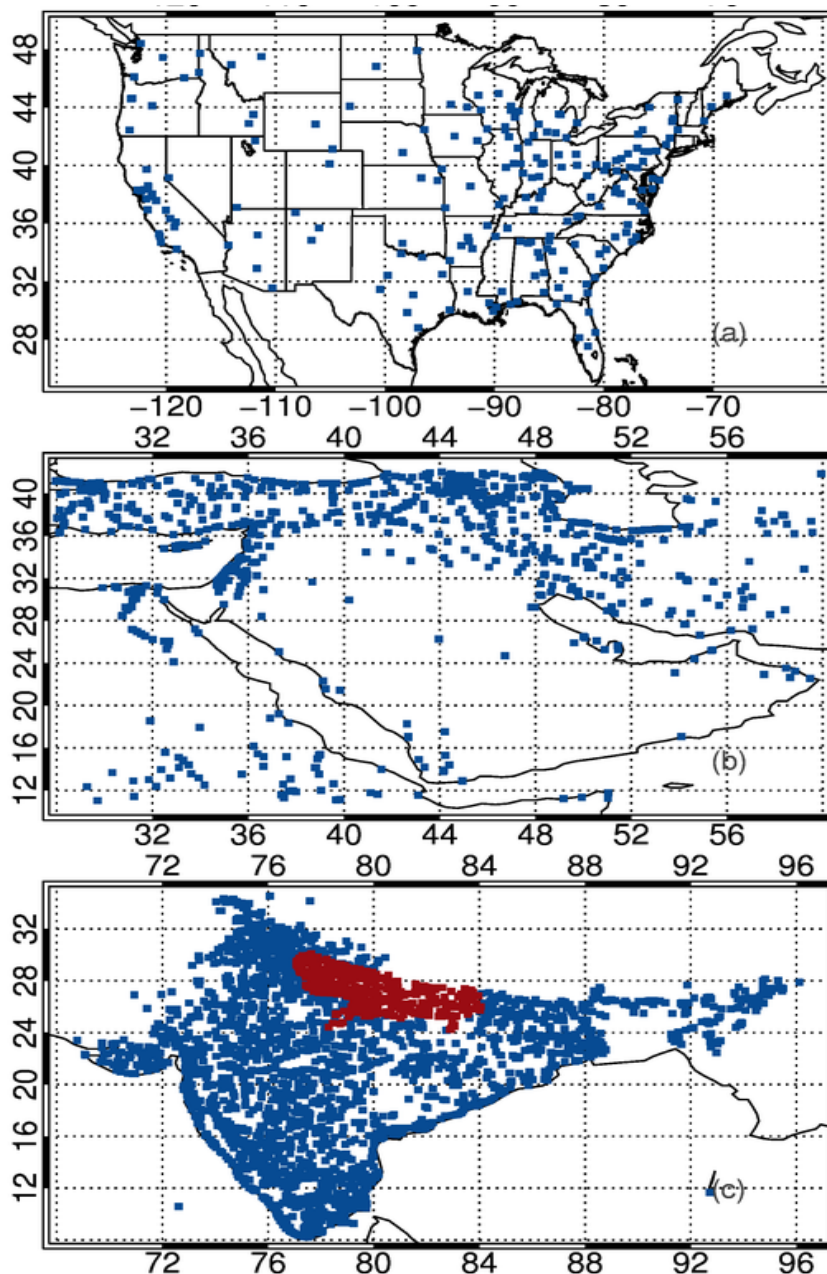


749 green, orange, and red colors represent AOT ranges of 0-0.2, 0.2-0.4, 0.4-0.6 and > 0.6,
750 respectively. (d) similar to (c) but for Jan. 16, 2015.

751

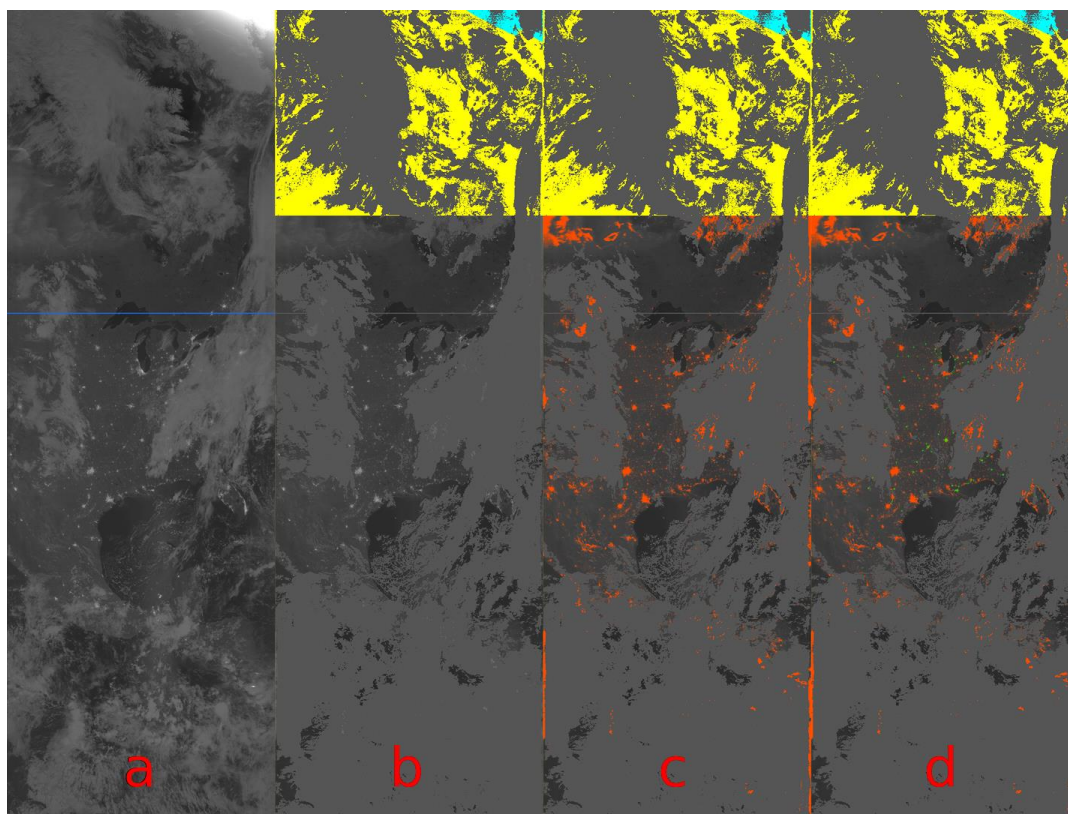
752 **Figure 11.** (a) Empirically derived (using data from Fig. 7d) and 6S model estimated diffuse
753 correction terms for the Middle East for 2015. (b): Similar to Fig. 10a but for the India region for
754 2015 (using data from Fig. 8d).

755



756

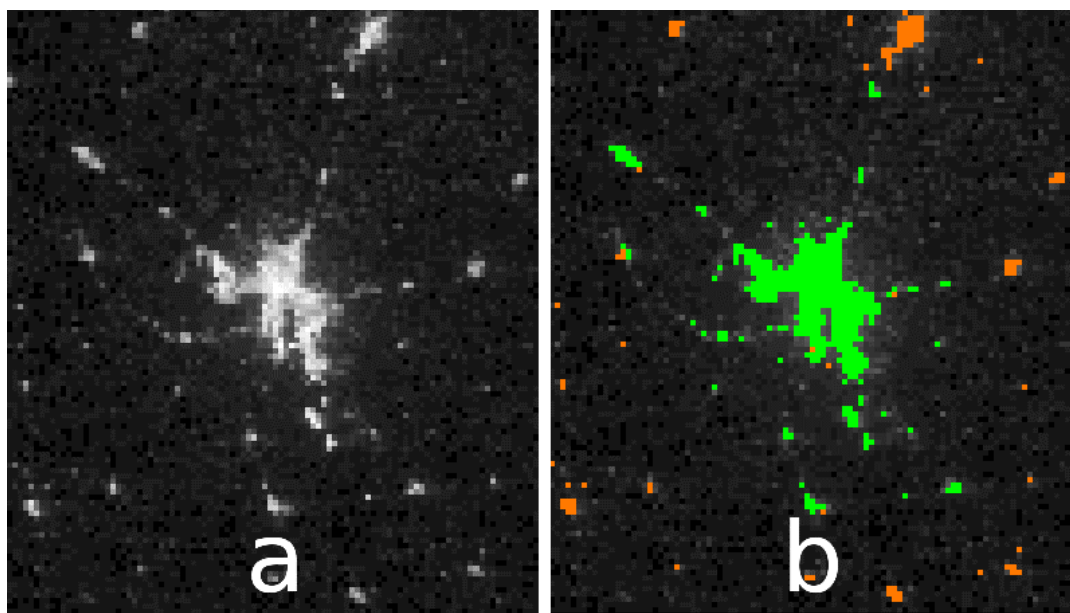
757 **Figure 1.** Spatial distribution of (a) 200 cities over the US, b). 999 cities over the Middle East,
758 and c) 2995 cities over India, used in this study. Red dots show cities/towns from the Uttar
759 Pradesh (UP) state of India—a region of climatologically high aerosol loading.



760

761 **Figure 2.** (a) VIIRS DNB contrast-enhanced imagery centered over North America from the
762 VIIRS DNB for October, 1 2015. (b) Same as (a), but with cloud screening and quality assurance
763 steps applied for cloudy (grey), saturated pixels (yellow), and solar zenith angle $s < 102^\circ$ (cyan).
764 (c) Similar to (b), but with artificial light sources identified through a granule level detection
765 (orange). (d) Similar to (c) but showing artificial light sources cross checked with a known city
766 database and through a regional level detection (green).

767



768

769

770 **Figure 3.** (a) VIIRS nighttime imagery on April 13, 2015 over Sioux City, Iowa, US. b) Similar
771 to (a) but showing detected artificial light sources using data within $\pm 0.3^\circ$ (Latitude/Longitude) of
772 the city center (green). Orange colors show the detected artificial light sources through a granule
773 level detection. Only green pixels are utilized for aerosol retrievals.

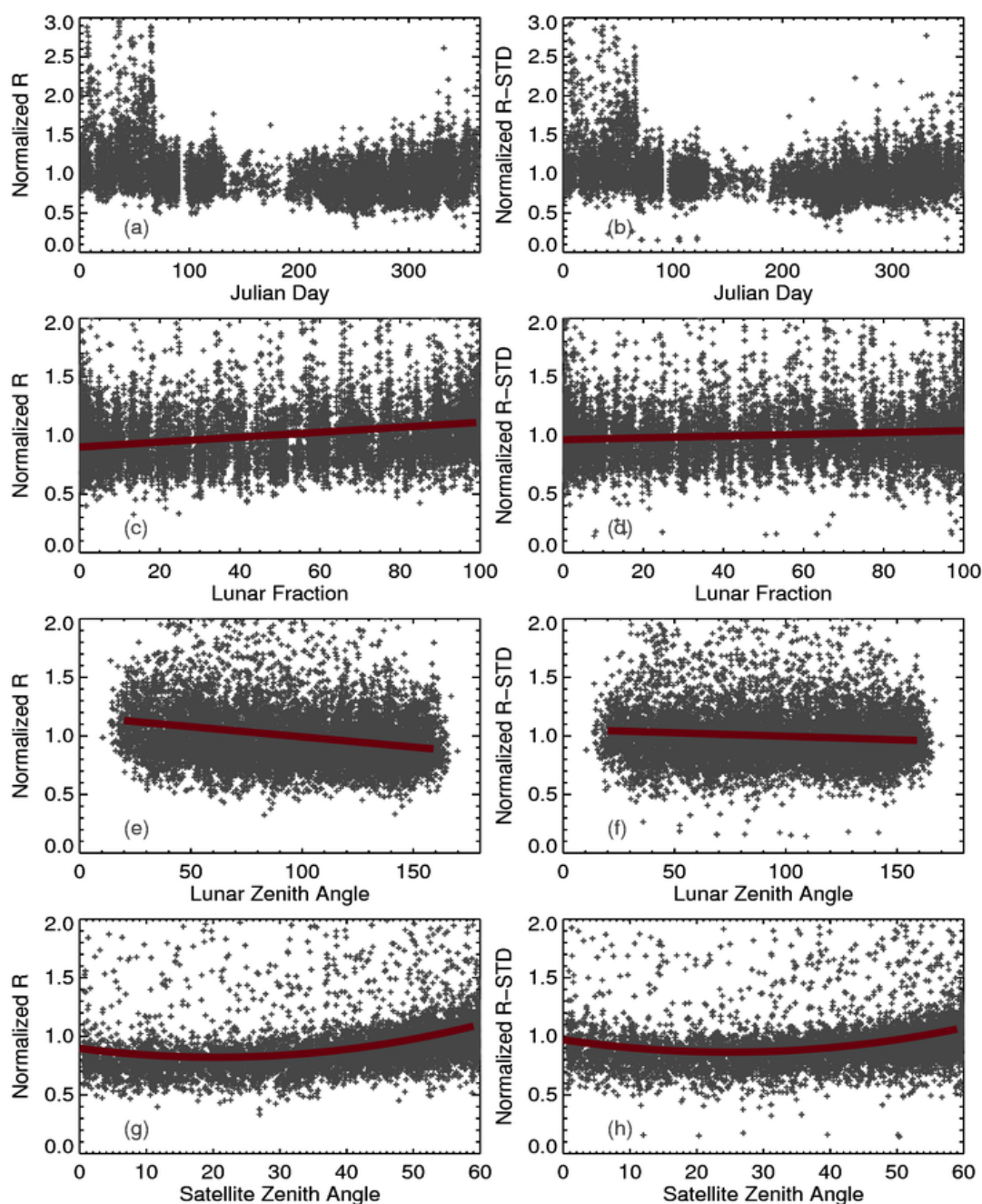
774

775

776

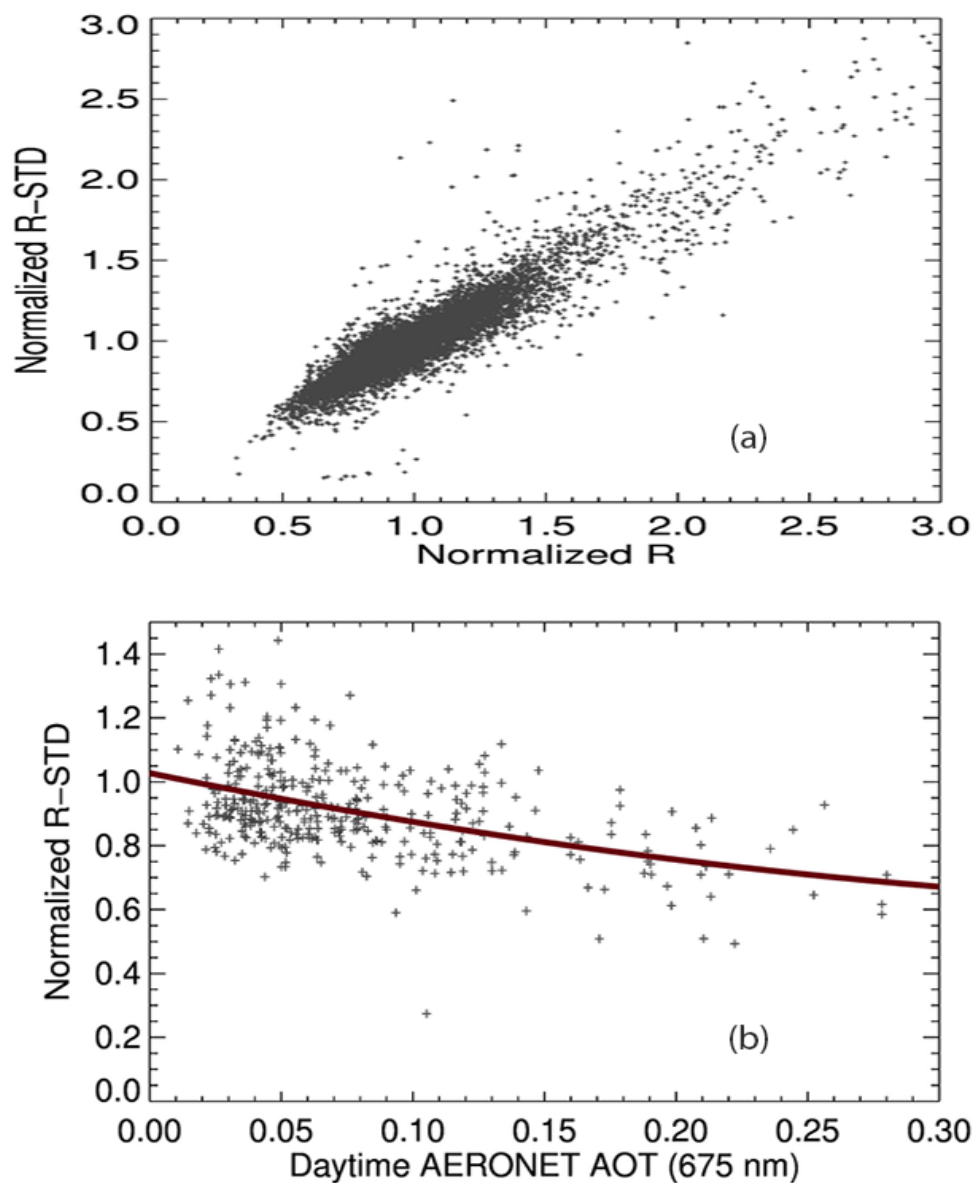
777

778



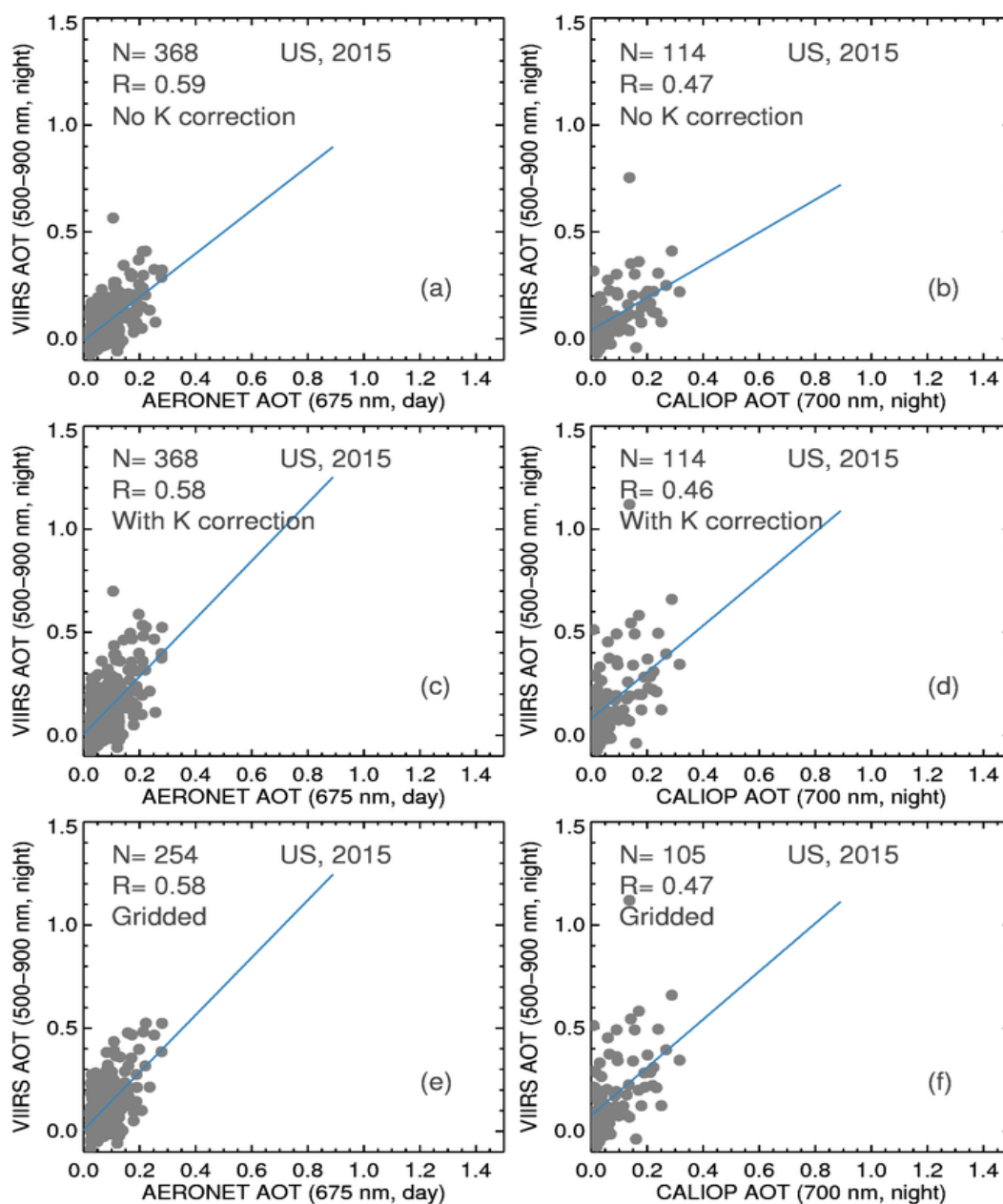
779

780 **Figure 4.** (a), (c), (e), and (g) show the normalized radiance of artificial light sources (200 selected
781 cities over the US, for 2015) as functions of Julian day, lunar fraction, lunar zenith angle, and
782 satellite zenith angle, respectively. (b), (d), (f), and (h) show the corresponding normalized
783 standard deviation of radiance for artificial light sources.



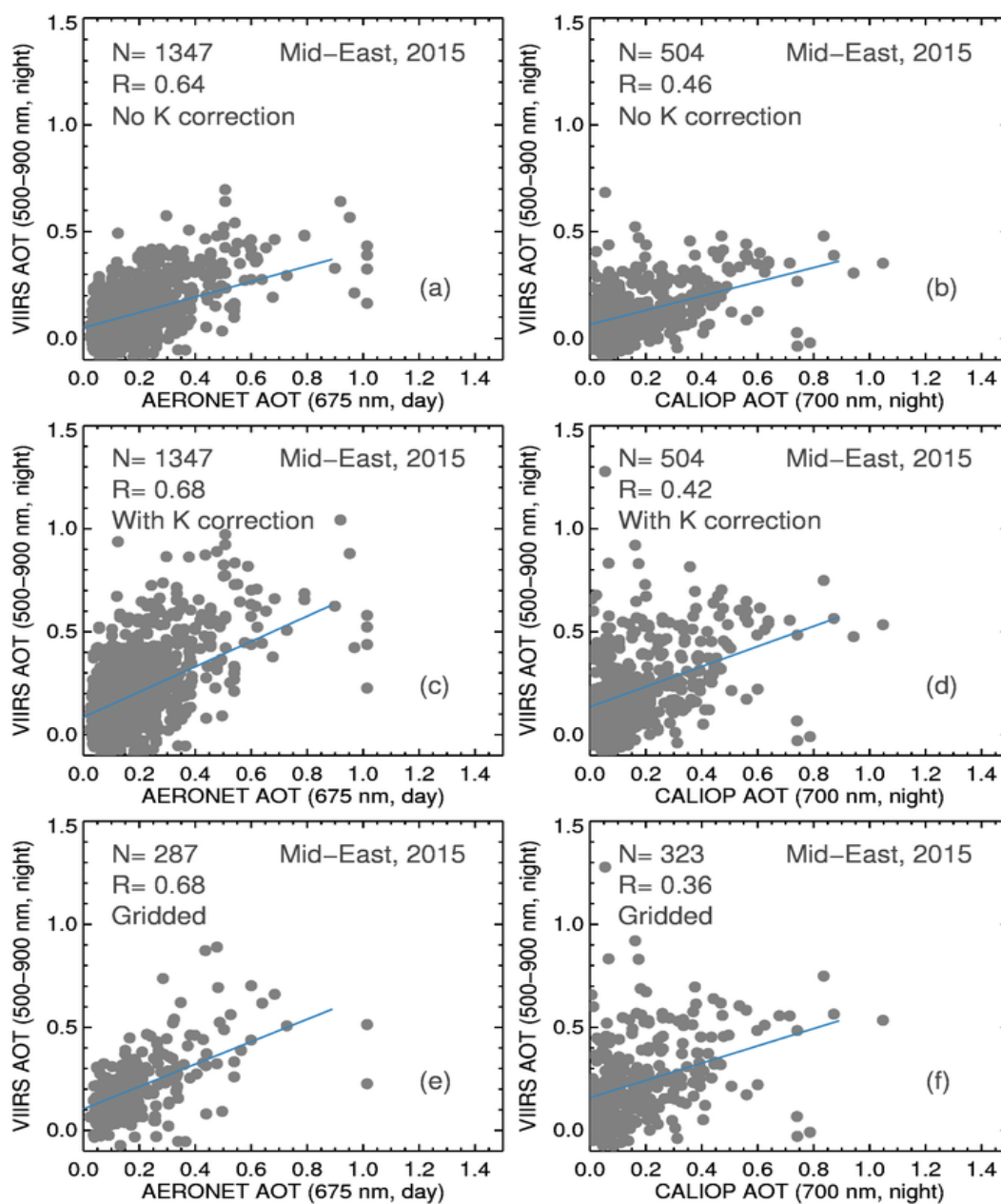
784

785 **Figure 5.** (a) Normalized radiance versus normalized standard deviation of radiance for 200 cities
786 over the US for 2015. (b) The normalized standard deviation of radiance as a function of adjacent
787 daytime AERONET AOT (0.675 μm).



788

789 **Figure 6.** (a) Scatter plot of VIIRS nighttime AOT versus adjacent daytime AERONET AOT
 790 (0.675 μm) for 200 selected cities over the US for 2015. No diffuse correction is applied. b)
 791 Similar to (a) but for using nighttime CALIOP AOT (0.7 μm). (c) and (d)) Similar (a) and (b) but
 792 with the diffuse correction implemented. (e) and (f): Similar to Figs. 6c and 6d but for gridded
 793 VIIRS data (averaged into $1^\circ \times 1^\circ$ Latitude/Longitude grids). Artificial light sources with fewer
 794 than 20 nights that passed various cloud screening and QA checks are excluded.

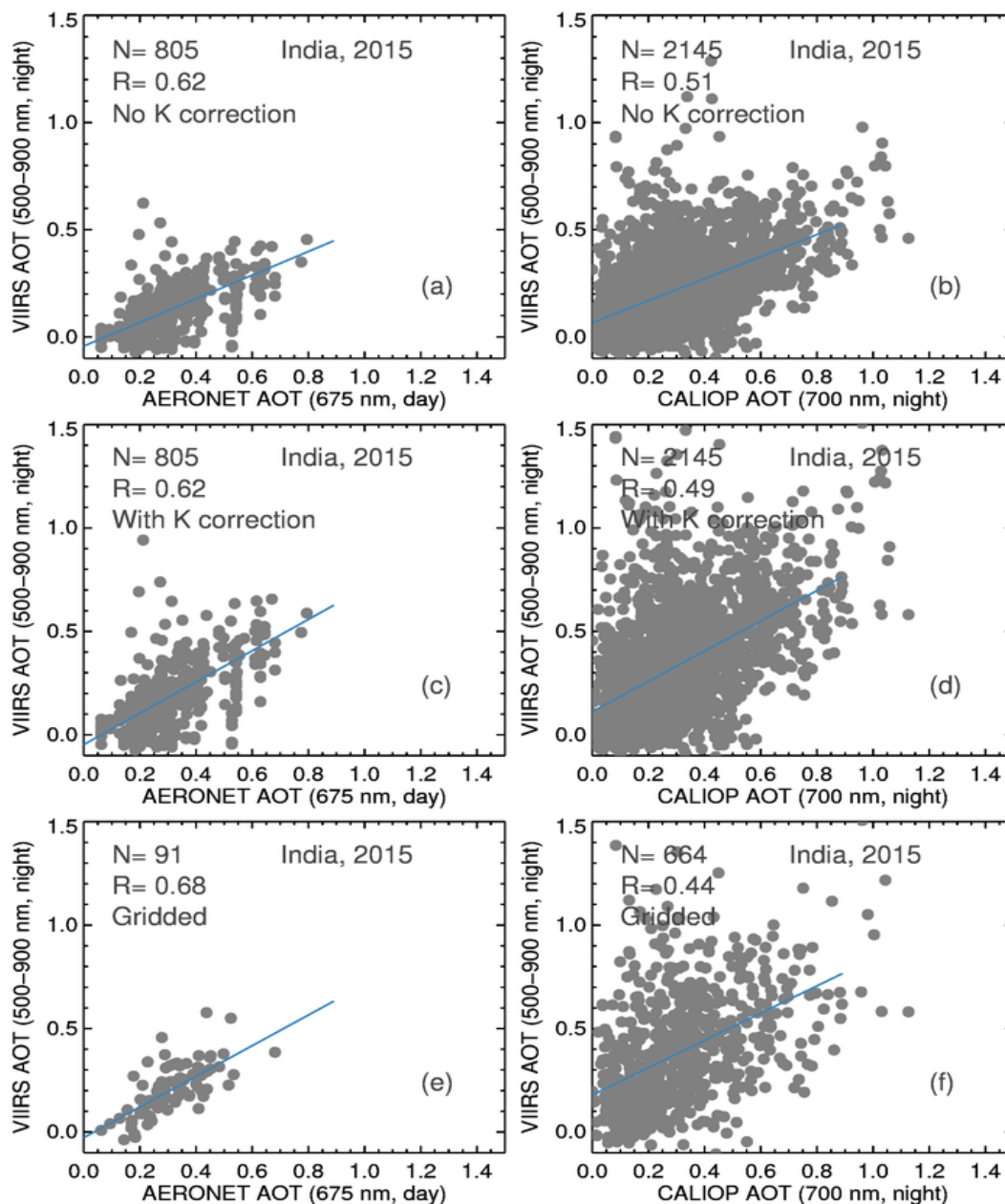


795

796 **Figure 7.** Similar to Fig. 6 but for 999 cities over the Middle East for 2015.

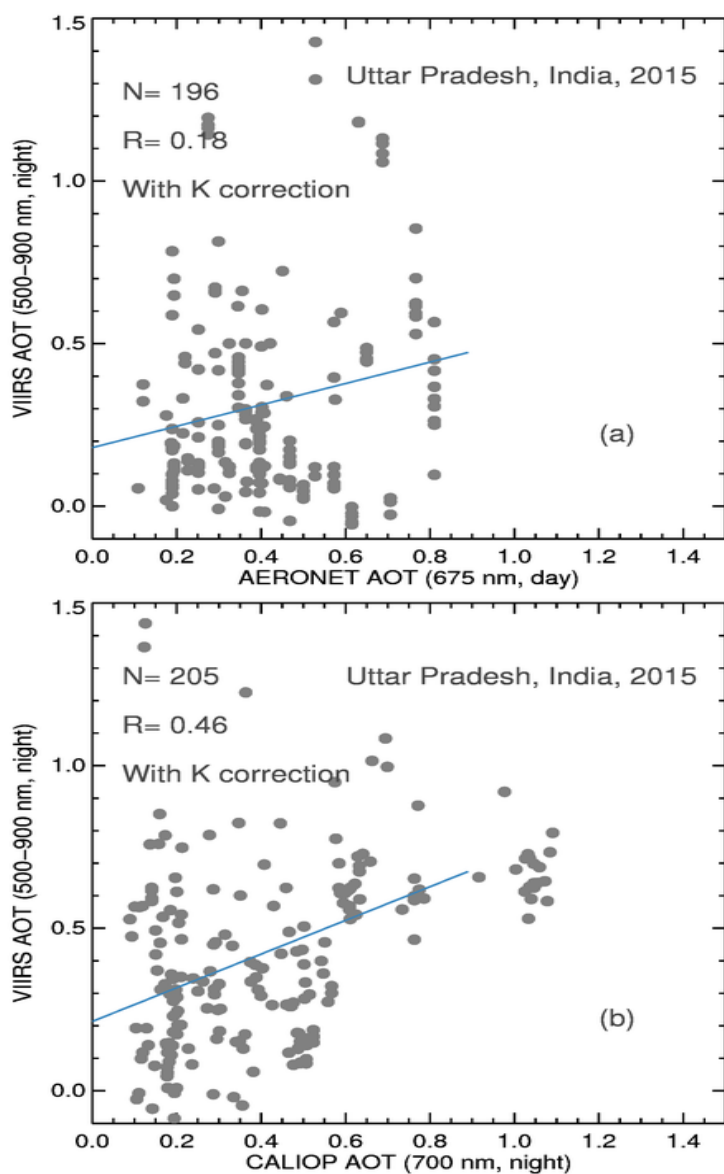
797

798



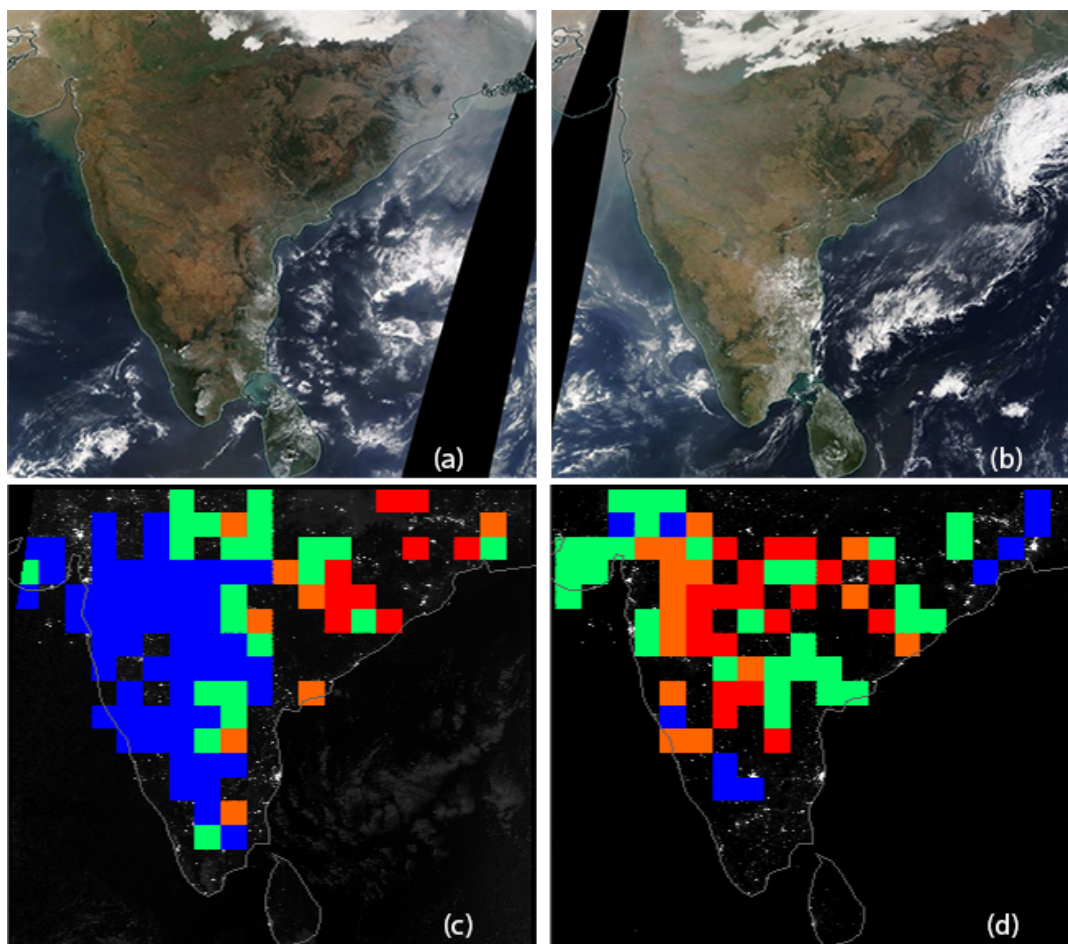
799
 800
 801
 802
 803

Figure 8. Similar to Fig. 7 but for the India region for 2015. Artificial light sources from the Uttar Pradesh State of India are excluded.



804
805
806
807
808
809

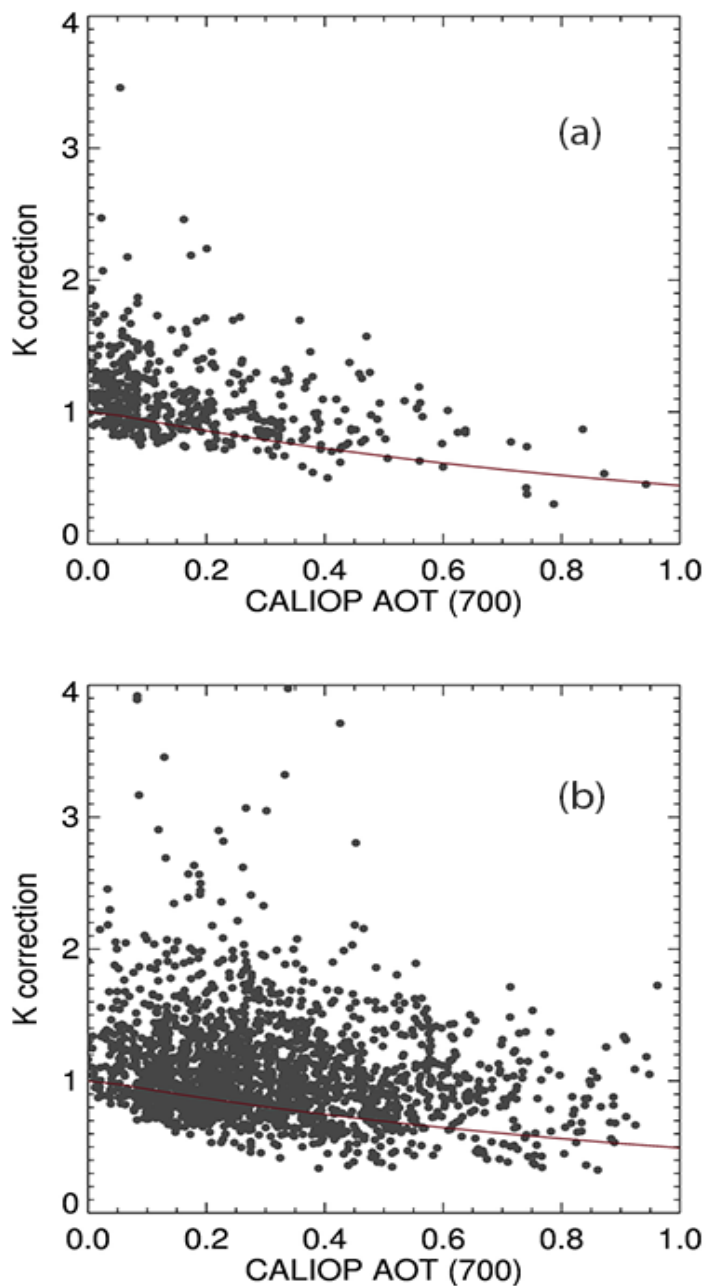
Figure 9. (a) Scatter plot of VIIRS nighttime AOT versus adjacent day time AERONET AOT (0.675 μm) over the Uttar Pradesh State of India for 2015. Diffuse correction is applied. (b): similar to (a), but for using nighttime CALIOP AOT (0.7 μm).



810
811 **Figure 10.** Terra MODIS true color imagery (NASA Worldview) for Jan. 12, 2015 over India.
812 (b): Similar as (a) but for Jan. 16, 2015. (c): VIIRS nighttime imagery on Jan. 12, 2015. Over
813 plotted are VIIRS nighttime AOT retrievals in $1^\circ \times 1^\circ$ (Latitude/Longitude) grid format. Blue,
814 green, orange, and red colors represent AOT ranges of 0-0.2, 0.2-0.4, 0.4-0.6 and > 0.6 ,
815 respectively. (d) similar to (c) but for Jan. 16, 2015.

816

817



818

819 **Figure 11.** (a) Empirically derived (using data from Fig. 7d) and 6S model estimated diffuse
820 correction terms for the Middle East for 2015. (b): Similar to Fig. 10a but for the India region for
821 2015 (using data from Fig. 8d).